In vivo imaging of corneal nerves and cellular structures in mice with Gabor-domain optical coherence microscopy

CRISTINA CANAVESI,[1,*] [ID] ANDREA COGLIATI,[1] AMANDA MIETUS,[2] YUE QI,[3] JESSE SCHALLEK,[4,5,6] JANNICK P. ROLLAND,[1,2] AND HOLLY B. HINDMAN[7]

[1] *LightTopTech Corp., 150 Lucius Gordon Dr Ste 201 West Henrietta, NY 14586-9687, USA*

[2] *University of Rochester, The Institute of Optics, 275 Hutchison Road, Rochester, NY 14627, USA*

[3] *University of Rochester, Department of Biomedical Engineering, 275 Hutchison Road, Rochester, NY 14627, USA*

[4] *University of Rochester Medical Center, Department of Ophthalmology, 601 Elmwood Ave, Rochester, NY 14642, USA*

[5] *University of Rochester, Center for Visual Science, 601 Elmwood Ave, Rochester, NY 14642, USA*

[6] *University of Rochester Medical Center, Department of Neuroscience, 601 Elmwood Avenue - Box 603, Rochester, New York 14642, USA*

[7] *The Eye Care Center, 325 West St, Canandaigua, NY 14424, USA*

*cristina@lightoptech.com

Abstract: Gabor-domain optical coherence microscopy (GDOCM) demonstrated *in vivo* corneal imaging with cellular resolution and differentiation in mice over a field of view of 1 mm^2. Contact and non-contact imaging was conducted on six healthy and six hyperglycemic C57BL/6J mice. Cellular resolution in the 3D GDOCM images was achieved after motion correction. Corneal nerve fibers were traced and their lengths and branches calculated. Noncontact, label-free imaging of corneal nerves has clinical utility in health and disease, and in transplant evaluation. To the authors' knowledge, this is the first report of *in vivo* 3D corneal imaging in mice with the capability to resolve nerve fibers using a non-contact imaging modality.

1. Introduction

Noninvasive imaging plays an increasingly important role in early detection and longitudinal monitoring of disease. Noninvasive imaging is especially needed for the cornea, the outermost window of our visual system, since removing a sample for histologic evaluation would result in irreversible damage and vision loss. Various types of infections and diseases affecting the cornea constitute the second cause of blindness worldwide [1]. Corneal dystrophies affect nearly 300,000 people in the United States, with Fuchs' dystrophy affecting 4% of people aged over 40 and being the leading cause of transplant worldwide [2–4]. Keratoconus causes thinning, protrusion and scarring of the cornea, resulting in distorted vision; it has an estimated prevalence of 54 per 100,000 and accounts for nearly one third of the global annual ~185,000 corneal transplants [4–6]. Dry eye disease is one of the most common reasons for seeking eye care and has prevalence rates ranging from 7% to 33% [7,8]. Corneal ectasia, a complication occurring after refractive surgery, causes progressing steepening and thinning of the cornea, and there is strong interest in understanding its risk factors [9,10]. Corneal neuropathy affects nearly 50% of patients with diabetes mellitus, a metabolic disease characterized by elevated blood glucose, which affects over 400 million people globally and over 9% of the population in the United States [11,12]. Diabetes causes a number of vascular complications, including diabetic retinopathy, the leading cause of blindness in individuals of working age in developed countries [13–15], and corneal neuropathy [16–18]. Importantly, changes in the corneal sub-basal nerves were shown

to precede other clinical and electrophysiological manifestations of neuropathy, indicating the possibility of corneal nerve imaging being a biomarker for assessment of diabetic neuropathy [19].

Corneal nerves have long been a challenge to study well *in vivo*, in light of their geometry of small thin fibers (ranging in diameter from 0.4 to 40.3 µm) forming a complex network through the corneal tissues [20]. Current options for *in vivo* corneal imaging include confocal microscopy and optical coherence tomography (OCT). Confocal microscopy has been used extensively to investigate the corneal nerves *in vivo* [21–30], and in the context of studying the changes induced with diabetes mellitus on corneal nerves in humans, mice and rats [19,31–36]. Patients with diabetes had reduced densities of major corneal nerves and nerve branching, as well as increased tortuosity [31,32]. Sub-basal layer corneal nerve density was reduced by over 30% in diabetic relative to control mice [33]. However, the challenges associated with the corneal contact required for the *in vivo* use of confocal microscopy and the small field of view make it difficult to assess the long and branching fibers that can extend over many fields of view and through various depths.

OCT is an optical imaging technique based on low-coherence interferometry that can achieve micron-scale axial resolution [37]. An advantage of OCT over confocal microscopy, in addition to the millimeter imaging depth capability, is that it enables non-contact operation; however, its lateral resolution is typically limited to 10-20 µm. To address the shortcomings of confocal microscopy, there has been interest in developing and demonstrating the capability to resolve corneal nerves *in vivo* using OCT [38,39], full-field OCT [40] and micro-OCT [41,42]. Werkmeister et al. [38] demonstrated the capability to visualize corneal nerves in humans *in vivo* using ultrahigh-resolution OCT with axial resolution of 1.2 µm (in tissue) and lateral resolution of 20 µm, and field of view of 7.5×7.5 mm^2. Since the thickness of the nerves (5-10 µm) was below the lateral resolution of the system, the nerves were only visible in the B-scans. Shin et al. [39] developed an OCT system with axial resolution of 8.8 µm (in air) and lateral resolution of 21 µm, over a field of view of 10×10 mm^2; after motion correction and image processing, nerve fibers with diameter ~20 µm were visible in the *en face* view. Mazlin et al. [40] reported the first *in vivo* imaging of human cornea using a full-field OCT system with axial resolution of 7.7 µm and lateral resolution of 1.6 µm over a field of view of 1.26×1.26 mm^2. Various features of interest in the sub-basal nerve plexus and stroma, including hyper-reflective branching nerves with thickness of 3-8 µm and an 80 µm-thick stromal node connecting four nerves with individual thickness of 10 µm, were clearly visible. However, volumetric images could not be produced due to the need to adjust the reference arm for each axial position. Tan et al. demonstrated *in vivo* OCT imaging of human corneas with isotropic 1.5 µm resolution at an A-scan rate of 250 kHz over a field of view of 0.75×0.75 mm^2 [41]. Reflective sub-basal corneal nerves were clearly visible, yet the imaging was limited to a depth of ~20 µm due to the high NA of the objective (0.26). Chen et al. [42] demonstrated visualization of nerve fibers with *ex vivo* imaging of mouse and rat corneas, and *ex vivo* and *in vivo* imaging of minipig corneas using a micro-OCT (µOCT) system with axial resolution of 1.6 µm (in air) and lateral resolution of 2.4 µm over a field of view of 0.872×0.872 mm^2; a limitation of µOCT is its shallow depth of focus (30-40 µm).

Gabor-domain optical coherence microscopy (GDOCM) was introduced to produce cellular resolution imaging in 3D over a depth of imaging comparable to that of conventional OCT [43,44]. It leverages a high numerical aperture microscope with an integrated liquid lens for dynamic refocusing, resulting in 2 µm isotropic resolution in the volume being imaged, over a 1 mm $\times$ 1 mm field of view, and depth of imaging up to 2.5 mm in tissue [44]. GDOCM achieves volumetric imaging with invariant resolution by acquiring multiple 3D images at different focal depths and fusing together the in-focus portions of each image [43–45]. Dynamic focusing with no moving parts is achieved with a liquid lens embedded in the GDOCM microscope probe [46]. A dual-axis micro-electro-mechanical system (MEMS) is used to scan the beam over a field of view of 1 mm^2 [47].

Prior *in vivo* application to skin imaging with GDOCM demonstrated an ability to detect and differentiate atypical basal cells from normal skin morphology using a contact imaging modality [48]. GDOCM has already been shown to provide cellular resolution imaging in 3D on corneal tissue with *ex vivo* corneas using the contact imaging modality [49–52], in particular to study endothelial cells [51–53]. However, high quality corneal images are difficult to attain *in vivo* with contact imaging, in light of the high sensitivity of the cornea and resultant discomfort to the subject. The goal of this work is to develop and demonstrate non-contact *in vivo* corneal imaging that can provide a path for future translation of GDOCM to clinical applications.

In this study, we investigate GDOCM's capability to image corneal tissue with cellular resolution and to resolve corneal nerves in normal and diabetic mice *in vivo*. Herein, we describe our process for obtaining the first ever GDOCM *in vivo* corneal images. These were obtained using both contact and non-contact imaging modalities and in 3D. Methods for motion correction were applied to the images to correct for motion artifact resulting from *in vivo* imaging. 3D volumetric images were obtained of the corneas of diabetic and non-diabetic mice. The corneal nerves were then traced and their lengths compared with an interest in exploring the possibility of differentiating healthy corneal nerves from diseased based on these anatomical differences.

2. Animal models

All animal studies were performed in accordance to the guidelines of the National Institutes of Health with protocols approved by the University Committee on Animal Resources at the University of Rochester. Two sets of male mice were imaged: a control group comprised of C57BL6/J mice aged 2-3 months (000664; Jackson Laboratory, Bar Harbor, ME, USA) and a group of hyperglycemic mice ("diabetic mice") aged 12-13 months, because the loss of nerve fibers in the cornea was shown not to be detected until 20 weeks of hyperglycemia [33]. Two diabetic mouse populations were imaged based on their established utility in the diabetic modeling community. The two models reduce insulin as a result of two independent mechanisms of action. The first is the streptozotocin (STZ) induced model [54], in which a single intraperitoneal injection of streptozotocin at 150 mg/kg (S-0130; Sigma Aldrich) was given at least six months before imaging. The second model is the Ins2akita/J mouse (003548; Jackson Laboratory) that has a spontaneous mutation in the insulin 2 gene, leading to misfolding of insulin and resultant accumulation and toxicity in pancreatic ß cells [55]. Only male mice were used in this study due to the gender specificity of the hyperglycemic phenotype in the STZ and Ins2akita/J models [54,55].

Prior to imaging, mice were anesthetized using a mixture of ketamine (100 mg/mL) and xylazine (20 mg/mL) by an intraperitoneal injection with a 0.05 mL/g mouse weight. Mouse body temperature was controlled by placing the animal on a heat pad. Once the mouse was anesthetized, it was placed in a custom holder, with its teeth on a metal bite bar, and the holder was rotated to position the eye to be imaged to be orthonormal to the GDOCM microscope (see Fig. 2). Whiskers were kept out of the imaging path using GenTeal Tears Severe Dry Eye Gel lubricant (Alcon).

3. Results

3.1. *In vivo corneal imaging with Gabor-domain optical coherence microscopy*

The schematic of the Gabor-domain optical coherence microscopy system used in this study is shown in Fig. 1. The light source was a superluminescent diode with a FWHM bandwidth of 100 nm centered at 840 nm (BroadLighter D-840-HP-I, Superlum), which resulted in a theoretical axial point spread function of 2.2 μm in corneal tissue (average refractive index of 1.387 at 840 nm). The GDOCM system consisted of a Michelson interferometer with a 2×2 fiber optics coupler (TW850R5A2, Thorlabs) with a 50:50 split ratio. The reference arm includes

a polarization controller and a frequency domain delay line for dispersion compensation [56]. The microscope, located in the sample arm, incorporates a 2D MEMS mirror to scan over a 1 mm × 1 mm field of view, and a liquid lens for dynamic refocusing [46,47]. The microscope has a numerical aperture of 0.18, resulting in a lateral resolution of 2.85 μm. The spectrometer was based on a Czerny-Turner design, with a reflective grating (Newport) and a 4k-pixel line camera with maximum scan rate of 81 kHz (Piranha, Teledyne). For this study, the nominal A-scan rate used was 66 kHz, with a duty cycle, i.e., linear scanning portion, of 83.33%, resulting in an effective A-scan rate of 56 kHz [47].
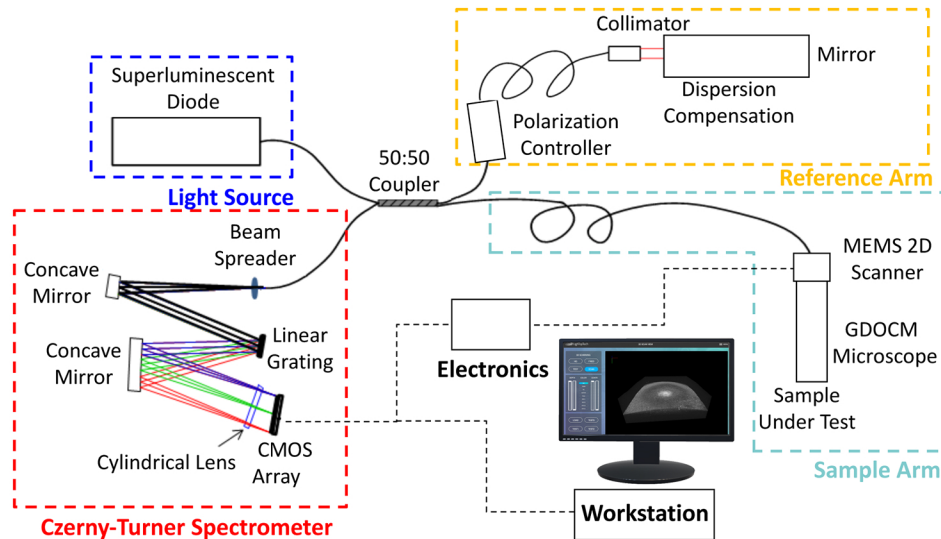

Fig. 1. Schematic of the Gabor-domain optical coherence microscopy (GDOCM) microscope. CMOS: Complementary metal oxide semiconductor; MEMS: Microelectromechanical systems.

To investigate the impact of motion and evaluate the possible translation to clinical applications in ophthalmology, *in vivo* GDOCM imaging of the mouse cornea was conducted for the first time in two imaging modalities: contact (optical contact between microscope and mouse cornea with GenTeal) and non-contact (15 mm working distance), as shown in Fig. 2. When imaging in non-contact mode, the eye being imaged was kept lubricated using drops of saline solution every 2-3 minutes. If the anesthesia duration allowed it (typically 25-45 minutes), both eyes were imaged in each mouse, each with a single imaging modality different from that of the other eye. Due to the shallow thickness of the mouse cornea (~100 μm), a single focusing depth of the liquid lens was used for image acquisition. A video feed produced by a 2D camera integrated with the GDOCM microscope was used to align the center of the mouse cornea to the center of the 1 mm × 1 mm field of view.

A total of 12 corneas were imaged for analysis: 4 control and 4 diabetic mice in contact, and 2 control and 2 diabetic mice in non-contact. Both sets of images (contact and non-contact) were impacted by motion artifacts caused by the mouse's heartbeat and respiration. The respiration rate in mice anesthetized with ketamine and xylazine is around 130-170 breaths/min (2.2-2.8 Hz), while the heart rate is 300-480 beats/min (5-8 Hz) [57], as described in previous studies by our group [58,59]. For an A-scan rate of 56 kHz, the acquisition of 1000 × 1000 A-scans results in a B-scan rate of 56 Hz, and a volume imaging rate of 0.056 Hz. The fast B-scan rate (depth cross-sections acquired along the fast axis of the scanning) was not significantly impacted by motion, however the C-scans (depth cross-sections in the direction of the slow axis of the
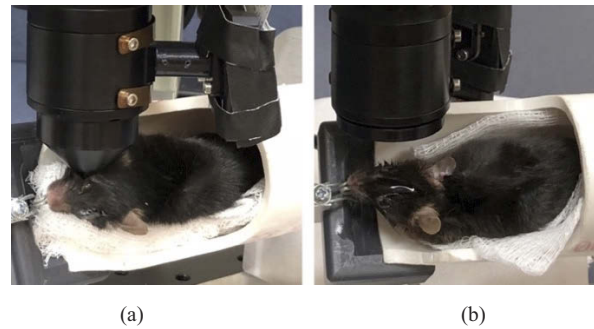
(a)   (b)

Fig. 2. (a) Contact and (b) non-contact imaging setup for GDOCM *in vivo* corneal imaging.

scanning) were on average impacted by 39-51 breaths and 90-144 heart beats over the 18 s acquisition time, and required motion correction.

3.2. Motion correction

Both imaging modalities were impacted by *in vivo* sample motion and required post-processing motion correction to recover cellular resolution. An intensity-based registration using rigid body transformations was used to perform motion correction via the StackReg plug-in for ImageJ [60,61]. The algorithm performs an automatic subpixel image registration that minimizes the mean square intensity difference between two adjacent frames (the B-scans). Starting from the center of the stack, the algorithm iteratively registers adjacent frames in ascending and descending orders. Examples of the C-scan and the *en face* view in correspondence of the endothelium before and after motion correction are shown in Fig. 3 for both contact and non-contact imaging modalities.
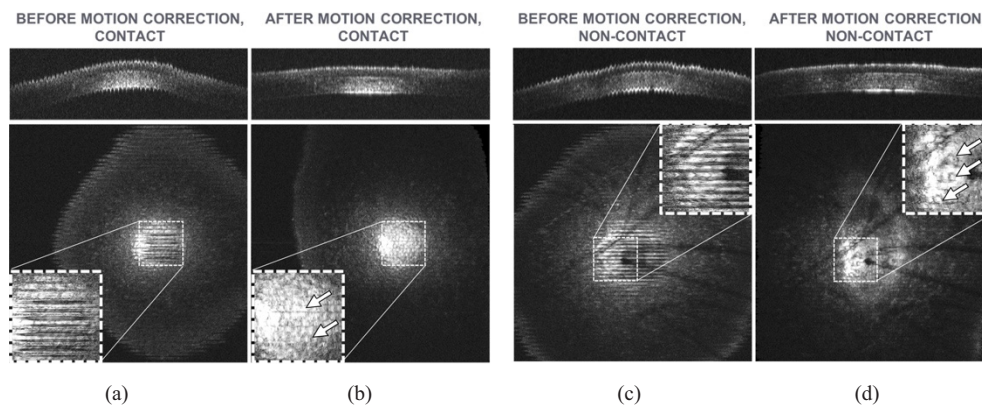

BEFORE MOTION CORRECTION, CONTACT   AFTER MOTION CORRECTION, CONTACT   BEFORE MOTION CORRECTION, NON-CONTACT   AFTER MOTION CORRECTION, NON-CONTACT

(a)   (b)   (c)   (d)

Fig. 3. Effects of motion during contact (a) and non-contact (c) imaging of mice cornea *in vivo*, and recovery of cellular resolution after motion correction (contact (b) and non-contact (d)). The field of view is 1×1 mm^2. Top figures = C-scans; bottom figures = *en face* views taken at the endothelium, the single layer of cells lining the posterior surface of the cornea; insets = magnified view showing amplitude of motion artifacts. Arrows in the insets on the *en face* views indicate endothelial cells. Images are brightest at the center due to the natural curvature of the cornea, which produces a stronger reflection at the center than at the periphery. The dark features in the non-contact images (c-d) are caused by mouse whiskers obscuring the view.

For the motion correction, we assumed that the dominant motion caused by the breathing and the heart beating was orthogonal to the scanning plane, i.e., orthogonal to the *en face* view and corresponding to the principal axis of the imaging system, since diaphragmatic movement had the greatest impact as the chest cavity moved in and out and changed the position of the anesthetized mouse cornea with respect to the microscope probe. Such Z-axis motion can be qualitatively confirmed by observing the motion pattern in the C-scans of Figs. 3(a) and 3(c). Only a translation on the Z-axis would be needed to compensate for such movements. However, no existing plugins were readily available to perform this registration, so more general transformations, i.e., rigid body transformations, were used. This approach is consistent with previous studies [62]. These transformations can correct axial motion as well as lateral motion along the fast axis of scanning. Intensity-based registration of medical volumes relies on the assumption that images from cross-sections that are close in space are highly similar, i.e., the majority of pixels in two adjacent cross-sections will have similar intensity; this was the case for the images in this study. One unintended effect of intensity-based registration of corneal images is that the curvature of the cornea along the C-scan axis is not preserved. The result of this can be observed in the C-scans of Figs. 3(b) and 3(d). This did not have a negative impact on this study.

For both imaging modalities, cellular features were recovered after motion correction, as exemplified by the mosaic of cells visible in the epithelium and endothelium, as shown in Fig. 4. The corresponding 3D image is shown in Fig. 5.

The appearance of basal epithelial cells as a mosaic of hypo-reflective cells with hyper-reflective borders and of endothelial cells as a regular mosaic of hexagonal hyper-reflective cells with hypo-reflective borders is consistent with findings typical of confocal microscopy [21].

3.3. Contact and non-contact in vivo imaging of corneal nerves in mice

Both contact and non-contact *in vivo* imaging modalities demonstrated the capability to resolve corneal nerves without applied contrast agents. Representative *en face* views with visible hyper-reflective sub-basal nerves are shown in Fig. 6. Since each *en face* view in a 3D GDOCM image covers a depth of ~1.5 μm, only a portion of the nerve fibers is visible in each *en face*

(a)   (b)
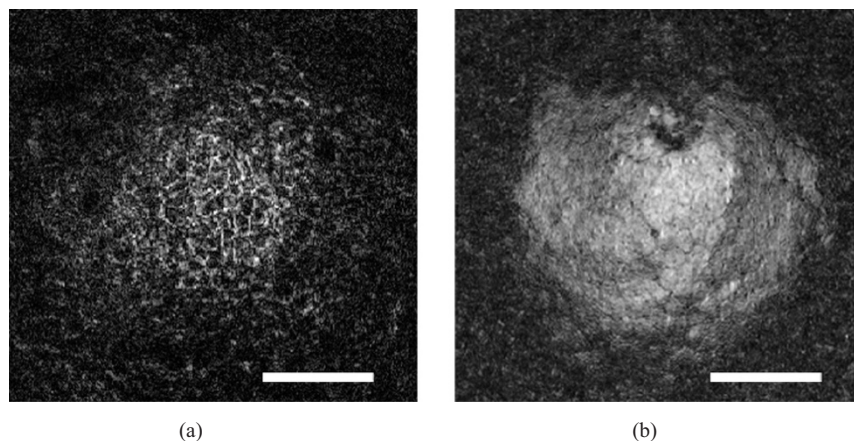
Fig. 4. Detail of the *en face* view of basal epithelial cells (a) and endothelial cells (b) imaged *in vivo* with GDOCM in a diabetic mouse in non-contact. The bar is 100 μm. Basal epithelial cells appear as a mosaic of dark cell bodies with light borders. Endothelial cells appear as a regular mosaic of hyper-reflective hexagonal cells surrounded by hypo-reflective borders. Sub-cellular imaging capability is demonstrated by the dark spots visible in some endothelial cells in (b), which are thought to be primary cilia [42,63].
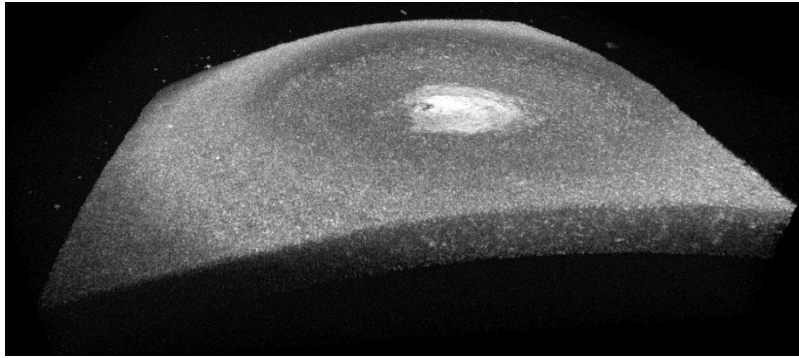
Fig. 5. 3D view of a cornea imaged *in vivo* with GDOCM in a diabetic mouse in non-contact over a 1 mm^2 field of view.

view. To our knowledge, this is the first report of *in vivo* 3D corneal imaging in mice with the capability to resolve nerve fibers using a non-contact imaging modality.
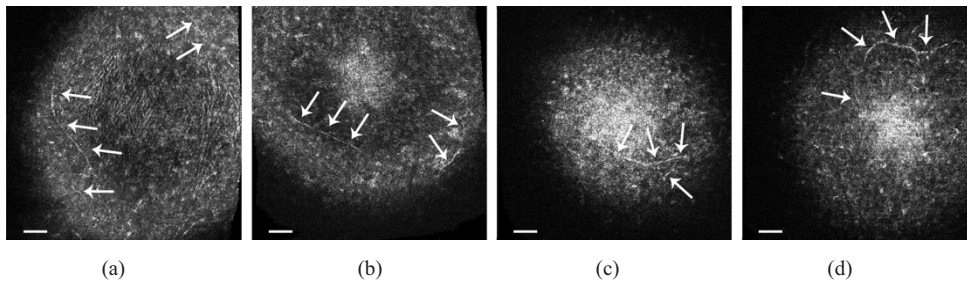

(a)   (b)   (c)   (d)

Fig. 6. Representative 1 mm × 1 mm *en face* views from different mice averaged over a depth of 6-13 μm, with corneal sub-basal nerves (arrows) visible after motion correction, using non-contact (a) and contact (b-d) imaging. The bar is 100 μm.

Corneal nerves could be observed clearly in the sub-basal layer and in the anterior stroma. Figure 7 shows some examples of nerve branching in the stroma.
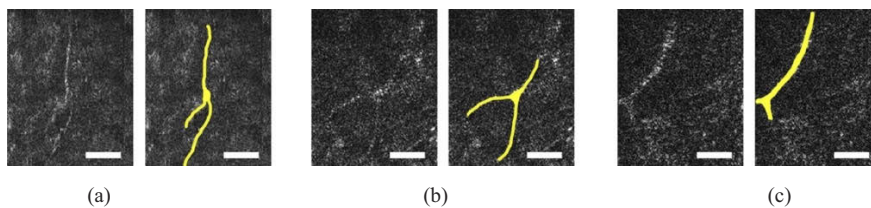

(a)   (b)   (c)

Fig. 7. GDOCM *en face* views showing details of single sub-basal nerve branching patterns for non-contact (a) and contact imaging (b, c). The nerves were highlighted in yellow on the right-hand side of each set of image pairs. The bar is 50 μm.

The "Simple Neurite Tracer" plugin in Fiji/ImageJ was used to trace the nerves in the motion-corrected 3D GDOCM images using a semi-automatic procedure [64]. Figure 8 shows the nerves traced for all images, overlaid with a representative *en face* view. The total lengths of the nerves were then computed, and the number of nerve branchpoints in each of the images counted.

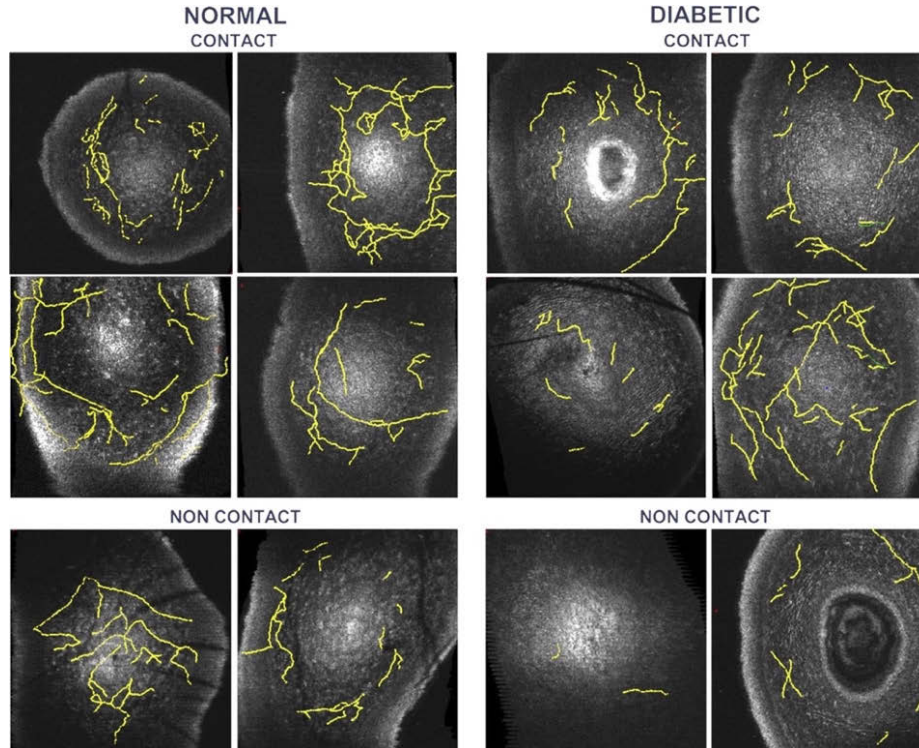The results of the traced nerve fiber lengths are reported in Table 1.

Fig. 8. Corneal sub-basal and stromal nerves (yellow) traced in the 3D GDOCM images overlaid with a representative *en face* view. The field of view is 1 mm × 1 mm.

Table 1. Total nerve length (in μm) measured from GDOCM in vivo mice corneal imaging for a total of n = 12 corneas.

Animal Population, Imaging Modality	Total Corneal Nerve Length (in μm)				Average Corneal Nerve Length (in μm)
Control, In Contact (n = 4)	3796	4302	7975	8177	6062 ± 2336
Diabetic, In Contact (n = 4)	1313	3614	4295	7755	4244 ± 2666
Control, Non-Contact (n = 2)		2984	5089		4037 ± 1489
Diabetic, Non-Contact (n = 2)		342	1629		985 ± 910

The number of branching points is reported in Table 2.

Table 2. Number of branching points measured from GDOCM in vivo mice corneal imaging for a total of n = 12 corneas.

Animal Population, Imaging Modality	Number of Branching Points				Average
Control, In Contact (n = 4)	6	17	14	34	18 ± 11.8
Diabetic, In Contact (n = 4)	3	10	13	20	12 ± 7
Control, Non-Contact (n = 2)	7		15		11 ± 5.7
Diabetic, Non-Contact (n = 2)	0		3		2 ± 2.1

In our limited sample size study, both the total nerve fiber length and the number of nerve branching points were lower in diabetic mice as compared to controls. This finding was consistent for corneas imaged by both contact and non-contact *in vivo* imaging modalities, as shown in Figs. 9 and 10. In the case of the contact imaging modality, the reduction in average total nerve fiber length observed was 30%, while in the non-contact imaging modality it was 76%. The number of branching points in diabetic corneas was reduced by 33% for contact imaging and by 82% for non-contact imaging.
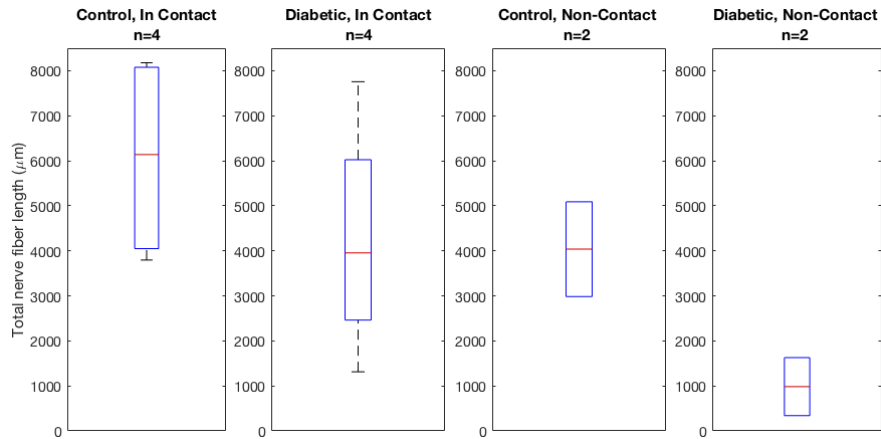

Fig. 9. Total nerve fiber length (in μm) in diabetic mice compared to normal in both contact and non-contact in vivo GDOCM imaging modalities.

We performed an unpaired T-test (one-tailed) comparing normal and diabetic mice. For contact imaging, the p-values were 0.173 and 0.203 for the nerve length and branching points, respectively. For non-contact imaging, the p-values were 0.079 and 0.112 for the nerve length and branching points, respectively.
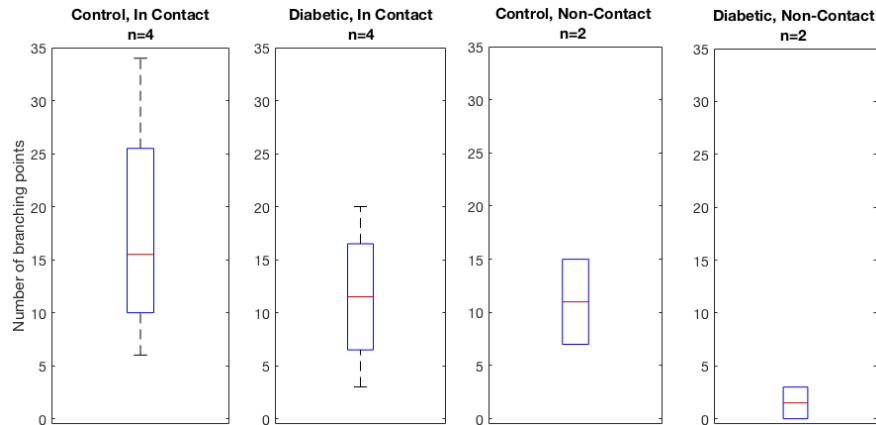
Fig. 10. Number of branching points in diabetic mice compared to normal in both contact and non-contact in vivo GDOCM imaging modalities.

4. Discussion

This study was the first demonstration of 3D *in vivo* corneal imaging with GDOCM, and the first demonstration of non-contact imaging of corneal nerves *in vivo* in mice, each representing a significant advance in the field.

Imaging healthy and diabetic mice *in vivo* with GDOCM, we used the intrinsic contrast of corneal nerves to study the impact of hyperglycemia on nerve density in corneal tissue. Misra et al. have suggested the possibility of using corneal nerve imaging as a biomarker for early detection of diabetic neuropathy [19]. It is possible that anatomical changes in the corneal nerves can precede physiological impairments, as confocal microscopy of corneal nerves can reveal diabetic nerve fiber damage earlier than corneal sensation testing and vibration perception assessment in the lower extremities [31]. Corneal nerve length has also been correlated with diabetic retinopathy with a statistically significant reduction in corneal nerve fiber length seen in diabetic patients with proliferative and non-proliferative retinopathy compared to diabetic patients with no diabetic retinopathy [32].

Our findings of decreased corneal nerve length and branching, although on a very limited sample size, are consistent with previous reports in the literature. Yorek et al. observed gradual loss of corneal nerves in diabetic mice, which reached statistical significance after 20 weeks from induction of diabetes [33]. Davidson et al. studied the impairment of corneal innervation in a diabetic rat model [34]. In this study, corneal nerve lengths and branching points were studied in healthy and diabetic mice to assess whether alterations in corneal nerve structure could be resolved in states of disease relative to health. We observed a reduction in corneal fiber length and in branching points in diabetic mice of over 30%. Similar reductions in corneal nerve length and branchings have been previously reported using *in vivo* confocal microscopy [31–33,65]. Our study was not designed nor powered to determine whether diabetic nerve lengths differ from normal nerve lengths, whether the different diabetic mice types have different corneal nerve findings, or whether differences in corneal nerve lengths have any have physiological significance, however we do show a viable quantification approach that will lend this technology to future detailed study of diabetic disease on nerve density of the cornea. Additionally, it should be noted that the control mice were much younger than diabetic mice due to availability of animals for the study, therefore mouse age is a possible confounder in the differences in nerve fiber length that were observed; however, it was previously reported that age does not impact nerve fiber density in a statistically significant manner both in mice [26] and in humans [66]. Our

goal was to demonstrate that quantitative data could be derived from the GDOCM images and has the potential to differentiate health from disease states. Toward this end, we demonstrate the beginnings of a quantification strategy that can be applied non-invasively in both normal and diseased corneas, an essential application of this imaging technology toward translational medicine and diagnostics.

Relative to non-contact imaging, contact imaging resulted in neither a significant increase nor decrease in motion artifact. Therefore, we applied the same motion correction to both sets of images. The resulting image quality obtained from both modalities was relatively equal. However, in our subsequent analyses, we observed that when imaging with non-contact modality, the average nerve fiber length was shorter than the fiber length visible in the contact modality. We suspect that motion artifacts impact the non-contact modality more severely, and more sophisticated motion correction schemes may need to be explored. Alternative motion correction approaches requiring acquisition of a second volume swapping the fast and slow axis of scanning can be implemented, at the expense of doubling the total acquisition time [29]. The motion correction procedure used changed the shape of the cornea; should the volumetric shape of the cornea need to be preserved, a more complex registration procedure can be used: first, a B-scan in the direction of the slow axis of the scanning is acquired either before or after the acquisition of the volume; then this B-scan is used to estimate the curvature of the cornea along the C-scan axis; finally this curvature is applied to the registered volume to reconstruct the original shape [62]. Additionally, future work is needed to test the motion correction procedure on 3D images acquired with multiple focal depths, as required for thicker samples, such as human corneas. Implementation of corneal GDOCM for clinical use in humans will require implementing a headrest and a fixation target to minimize voluntary eye movements, as well as optimizing the acquisition time to ensure the image is minimally affected by involuntary movements (e.g., tremor, drift and microsaccades) [67]. Either sufficiently fast imaging speeds to mitigate eye motion or motion correction algorithms as reported here will be needed to compensate for the larger motion artifact anticipated with normal awake human eye movement [62].

5. Conclusions

In vivo corneal imaging was conducted for the first time with Gabor-domain optical coherence microscopy (GDOCM) on normal and diabetic mice, with both non-contact and contact imaging modalities. After image processing to correct for motion artifacts caused by the mouse's heartbeat and respiration, sufficient resolution to visualize nerve fibers in the 3D GDOCM images was recovered. Reductions in average nerve fiber length and in nerve branching points greater than 30% were observed in diabetic mice, which is consistent with corneal changes caused by diabetic neuropathy. While more studies are needed to better understand the impact of diabetes on corneal nerve structure and function, these findings suggest the potential for GDOCM to evaluate corneal alterations *in vivo*, which can be useful in the assessment of systemic diseases such as diabetes mellitus and potentially other ocular diseases such as corneal dystrophies and keratopathies, and pre- and post-surgical interventions [68].

Disclosures

CC: LighTopTech Corp. (I,E), AC: LighTopTech Corp. (E), AM, YQ, JS: LighTopTech Corp. (F), HBH: LighTopTech Corp. (C), JPR: LighTopTech Corp. (I,P).

References

1. J. P. Whitcher, M. Srinivasan, and M. P. Upadhyay, "Corneal blindness: A global perspective," Bull. World Health Organ. **79**(3), 214–221 (2001).
2. D. C. Musch, L. M. Niziol, J. D. Stein, R. M. Kamyar, and A. Sugar, "Prevalence of corneal dystrophies in the United States: Estimates from claims data," Invest. Ophthalmol. Visual Sci. **52**(9), 6959–6963 (2011).
3. A. O. Eghrari, S. A. Riazuddin, and J. D. Gottsch, "Fuchs Corneal Dystrophy," in *Progress in Molecular Biology and Translational Science* (Elsevier B.V., 2015), 134, pp. 79–97.
4. P. Gain, R. Jullienne, Z. He, M. Aldossary, S. Acquart, F. Cognasse, and G. Thuret, "Global survey of corneal transplantation and eye banking," JAMA Ophthalmol. **134**(2), 167–173 (2016).
5. J. H. Krachmer, R. S. Feder, and M. W. Belin, "Keratoconus and related noninflammatory corneal thinning disorders," Surv. Ophthalmol. **28**(4), 293–322 (1984).
6. M. Romero-Jiménez, J. Santodomingo-Rubido, and J. S. Wolffsohn, "Keratoconus: A review," Contact Lens Anterior Eye **33**(4), 157–166 (2010).
7. J. L. Gayton, "Etiology, prevalence, and treatment of dry eye disease," Clin. Ophthalmol. **3**(1), 405–412 (2009).
8. B. Miljanović, R. Dana, D. A. Sullivan, and D. A. Schaumberg, "Impact of Dry Eye Syndrome on Vision-Related Quality of Life," Am. J. Ophthalmol. **143**(3), 409–415.e2 (2007).
9. J. B. Randleman, M. Woodward, M. J. Lynn, and R. D. Stulting, "Risk Assessment for Ectasia after Corneal Refractive Surgery," Ophthalmology **115**(1), 37–50.e4 (2008).
10. M. R. Santhiago, N. T. Giacomin, D. Smadja, and S. J. Bechara, "Ectasia risk factors in refractive surgery," Clin. Ophthalmol. **10**, 713–720 (2016).
11. D. M. Nathan, "Diabetes: Advances in diagnosis and treatment," JAMA **314**(10), 1052–1062 (2015).
12. G. Bikbova, T. Oshitari, T. Baba, M. Bikbov, and S. Yamamoto, "Diabetic corneal neuropathy: Clinical perspectives," Clin. Ophthalmol. **12**, 981–987 (2018).
13. F. Semeraro, A. Cancarini, R. Dell'Omo, S. Rezzola, M. R. Romano, and C. Costagliola, "Diabetic retinopathy: Vascular and inflammatory disease," J. Diabetes Res. **2015**, 1–16 (2015).
14. R. Klein, B. E. K. Klein, S. E. Moss, M. D. Davis, and D. L. DeMets, "The Wisconsin Epidemiologic Study of Diabetic Retinopathy: IV. Diabetic Macular Edema," Ophthalmology **91**(12), 1464–1474 (1984).
15. D. S. Fong, L. P. Aiello, F. L. Ferris, and R. Klein, "Diabetic Retinopathy," Diabetes Care **27**(10), 2540–2553 (2004).
16. V. J. Vieira-Potter, D. Karamichos, and D. J. Lee, "Ocular Complications of Diabetes and Therapeutic Approaches," BioMed Res. Int. **2016**, 1–14 (2016).
17. M. E. Rosenberg, T. M. T. Tervo, I. J. Immonen, L. J. Muller, C. Gronhagen-Riska, and M. H. Vesaluoma, "Corneal structure and sensitivity in type 1 diabetes mellitus," Invest. Ophthalmol. Vis. Sci. **41**(10), 2915–2921 (2000).
18. B. S. Shaheen, M. Bakir, and S. Jain, "Corneal nerves in health and disease," Surv. Ophthalmol. **59**(3), 263–285 (2014).
19. S. L. Misra, J. P. Craig, D. V. Patel, C. N. J. McGhee, M. Pradhan, K. Ellyett, D. Kilfoyle, and G. D. Braatvedt, "In vivo confocal microscopy of corneal nerves: An ocular biomarker for peripheral and cardiac autonomic neuropathy in type 1 diabetes mellitus," Invest. Ophthalmol. Visual Sci. **56**(9), 5060–5065 (2015).
20. C. F. Marfurt, J. Cox, S. Deek, and L. Dvorscak, "Anatomy of the human corneal innervation," Exp. Eye Res. **90**(4), 478–492 (2010).
21. R. Alzubaidi, M. S. Sharif, R. Qahwaji, S. Ipson, and A. Brahma, "In vivo confocal microscopic corneal images in health and disease with an emphasis on extracting features and visual signatures for corneal diseases: A review study," Br. J. Ophthalmol. **100**(1), 41–55 (2016).
22. D. V. Patel and C. N. J. McGhee, "In vivo confocal microscopy of human corneal nerves in health, in ocular and systemic disease, and following corneal surgery: A review," Br. J. Ophthalmol. **93**(7), 853–860 (2009).
23. D. V. Patel and C. N. J. McGhee, "Quantitative analysis of in vivo confocal microscopy images: A review," Surv. Ophthalmol. **58**(5), 466–475 (2013).
24. D. V. Patel and C. N. J. McGhee, "Mapping of the Normal Human Corneal Sub-Basal Nerve Plexus by In Vivo Laser Scanning Confocal Microscopy," Invest. Ophthalmol. Visual Sci. **46**(12), 4485–4488 (2005).
25. L. Oliveira-Soto and N. Efron, "Morphology of corneal nerves using confocal microscopy," Cornea **20**(4), 374–384 (2001).
26. M. Reichard, M. Hovakimyan, R. F. Guthoff, and O. Stachs, "In vivo visualisation of murine corneal nerve fibre regeneration in response to ciliary neurotrophic factor," Exp. Eye Res. **120**, 20–27 (2014).

27. O. Stachs, A. Zhivov, R. Kraak, J. Stave, and R. Guthoff, "In vivo three-dimensional confocal laser scanning microscopy of the epithelial nerve structure in the human cornea," Graefe's Arch. Clin. Exp. Ophthalmol. **245**(4), 569–575 (2007).

28. S. Allgeier, A. Zhivov, F. Eberle, B. Koehler, S. Maier, G. Bretthauer, R. F. Guthoff, and O. Stachs, "Image reconstruction of the subbasal nerve plexus with in vivo confocal microscopy," Invest. Ophthalmol. Visual Sci. **52**(9), 5022–5028 (2011).

29. J. Kokot, A. Wylęgała, B. Wowra, Ł Wójcik, D. Dobrowolski, and E. Wylęgała, "Corneal confocal sub-basal nerve plexus evaluation: a review," Acta Ophthalmol. **96**(3), 232–242 (2018).

30. W. M. Petroll and D. M. Robertson, "In Vivo Confocal Microscopy of the Cornea: New Developments in Image Acquisition, Reconstruction, and Analysis Using the HRT-Rostock Corneal Module," Ocul. Surf. **13**(3), 187–203 (2015).

31. E. M. Messmer, C. Schmid-Tannwald, D. Zapp, and A. Kampik, "In vivo confocal microscopy of corneal small fiber damage in diabetes mellitus," Graefe's Arch. Clin. Exp. Ophthalmol. **248**(9), 1307–1312 (2010).

32. J. Hafner, M. Zadrazil, A. Grisold, G. Ricken, M. Krenn, D. Kitzmantl, A. Pollreisz, A. Gleiss, and U. Schmidt-Erfurth, "Retinal and corneal neurodegeneration and its association to systemic signs of peripheral neuropathy in type 2 diabetes," Am. J. Ophthalmol. **209**, 197–205 (2020).

33. M. S. Yorek, A. Obrosov, H. Shevalye, S. Lupachyk, M. M. Harper, R. H. Kardon, and M. A. Yorek, "Effect of glycemic control on corneal nerves and peripheral neuropathy in streptozotocin-induced diabetic C57Bl/6J mice," J. Peripher. Nerv. Syst. **19**(3), 205–217 (2014).

34. E. P. Davidson, L. J. Coppey, A. Holmes, and M. A. Yorek, "Changes in corneal innervation and sensitivity and acetylcholine-mediated vascular relaxation of the posterior ciliary artery in a type 2 diabetic rat," Invest. Ophthalmol. Visual Sci. **53**(3), 1182–1187 (2012).

35. K. Edwards, N. Pritchard, C. Poole, C. Dehghani, K. Al Rashah, A. Russell, R. A. Malik, and N. Efron, "Development of a Novel Technique to Measure Corneal Nerve Migration Rate," Cornea **35**(5), 700–705 (2016).

36. D. Cai, M. Zhu, W. M. Petroll, V. Koppaka, and D. M. Robertson, "The impact of type 1 diabetes mellitus on corneal epithelial nerve morphology and the corneal epithelium," Am. J. Pathol. **184**(10), 2662–2670 (2014).

37. D. Huang, E. A. Swanson, C. P. Lin, J. S. Schuman, W. G. Stinson, W. Chang, M. R. Hee, T. Flotte, K. Gregory, C. A. Puliafito, and J. G. Fujimoto, "Optical Coherence Tomography," Science **254**(5035), 1178–1181 (1991).

38. R. M. Werkmeister, S. Sapeta, D. Schmidl, G. Garhöfer, G. Schmidinger, V. Aranha dos Santos, G. C. Aschinger, I. Baumgartner, N. Pircher, F. Schwarzhans, A. Pantalon, H. Dua, and L. Schmetterer, "Ultrahigh-resolution OCT imaging of the human cornea," Biomed. Opt. Express **8**(2), 1221–1239 (2017).

39. J. G. Shin, H. S. Hwang, T. J. Eom, and B. H. Lee, "In vivo three-dimensional imaging of human corneal nerves using Fourier-domain optical coherence tomography," J. Biomed. Opt. **22**(1), 010501 (2017).

40. V. Mazlin, P. Xiao, E. Dalimier, K. Grieve, K. Irsch, J.-A. Sahel, M. Fink, and A. C. Boccara, "In vivo high resolution human corneal imaging using full-field optical coherence tomography," Biomed. Opt. Express **9**(2), 557–568 (2018).

41. B. Tan, Z. Hosseinaee, L. Han, O. Kralj, L. Sorbara, and K. Bizheva, "250 kHz, 1.5 um resolution SD-OCT for in-vivo cellular imaging of the human cornea," Biomed. Opt. Express **9**(12), 6569–6583 (2018).

42. S. Chen, X. Liu, N. Wang, X. Wang, Q. Xiong, E. Bo, X. Yu, S. Chen, and L. Liu, "Visualizing Micro-anatomical Structures of the Posterior Cornea with Micro-optical Coherence Tomography," Sci. Rep. **7**(1), 10752 (2017).

43. J. P. Rolland, P. Meemon, S. Murali, A. Jain, N. Papp, K. P. Thompson, and K.-S. Lee, "Gabor domain optical coherence microscopy," Proc. SPIE **7139**, 71390F (2008).

44. C. Canavesi and J. P. Rolland, "Ten Years of Gabor-Domain Optical Coherence Microscopy," Appl. Sci. **9**(12), 2565 (2019).

45. J. P. Rolland, P. Meemon, S. Murali, K. P. Thompson, and K. Lee, "Gabor-based fusion technique for Optical Coherence Microscopy," Opt. Express **18**(4), 3632–3642 (2010).

46. S. Murali, K. P. Thompson, and J. P. Rolland, "Three-dimensional adaptive microscopy using embedded liquid lens," Opt. Lett. **34**(2), 145–147 (2009).

47. A. Cogliati, C. Canavesi, A. Hayes, P. Tankam, V.-F. Duma, A. P. Santhanam, K. P. Thompson, and J. P. Rolland, "MEMS-based handheld scanning probe with pre-shaped input signals for distortion-free images in Gabor-domain optical coherence microscopy," Opt. Express **24**(12), 13365–13374 (2016).

48. P. Tankam, J. Soh, C. Canavesi, M. Lanis, A. Hayes, A. Cogliati, J. P. Rolland, and S. F. Ibrahim, "Gabor-Domain Optical Coherence Tomography to Aid in Mohs Resection of Basal Cell Carcinoma," J. Am. Acad. Dermatol. **80**(6), 1766–1769 (2019).

49. P. Tankam, Z. He, M. Lanis, C. Canavesi, T. Lepine, H. B. Hindman, D. Topham, G. Thuret, P. Gain, and J. Rolland-Thompson, "Assessing the microstructures of the human cornea using Gabor-Domain optical coherence microscopy with large field of view and high resolution," Invest. Ophthalmol. Visual Sci. **56**(7), 3164 (2015).

50. P. Tankam, Z. He, H. B. Hindman, C. Canavesi, J. Coyoc Escudero, T. Lepine, P. Gain, and J. P. Rolland, "Capabilities of Gabor-domain Optical Coherence Microscopy for the Assessment of Corneal Disease," J. Biomed. Opt. **24**(4), 1 (2019).

51. C. Yoon, A. Mietus, Y. Qi, J. J. Stone, J. Coyoc Escudero, C. Canavesi, P. Tankam, H. B. Hindman, and J. P. Rolland, "Quantitative assessment of human donor corneal endothelium with Gabor domain optical coherence microscopy," J. Biomed. Opt. **24**(08), 1 (2019).

52. P. Tankam, Z. He, Y.-J. Chu, J. Won, C. Canavesi, T. Lepine, H. B. Hindman, D. J. Topham, P. Gain, G. Thuret, and J. P. Rolland, "Assessing microstructures of the cornea with Gabor-domain optical coherence microscopy: pathway for corneal physiology and diseases," Opt. Lett. **40**(6), 1113–1116 (2015).

53. C. Canavesi, A. Cogliati, C. Yoon, A. Mietus, Y. Qi, J. J. Stone, H. Hindman, and J. P. Rolland, "3D cellular imaging of the cornea with Gabor-domain optical coherence microscopy," Proc. SPIE **10867**, 108670F (2019).

54. F. Brosius, "High-Dose Streptozotocin Induction Protocol (Mouse)," (2015).

55. A. J. Barber, D. A. Antonetti, T. S. Kern, C. E. N. Reiter, R. S. Soans, J. K. Krady, S. W. Levison, T. W. Gardner, and S. K. Bronson, "The Ins2Akita mouse as a model of early retinal complications in diabetes," Invest. Ophthalmol. Visual Sci. **46**(6), 2210–2218 (2005).

56. K.-S. Lee, A. C. Akcay, T. Delemos, E. Clarkson, and J. P. Rolland, "Dispersion control with a Fourier-domain optical delay line in a fiber-optic imaging interferometer," Appl. Opt. **44**(19), 4009–4022 (2005).

57. A. Tsukamoto, K. Serizawa, R. Sato, J. Yamazaki, and T. Inomata, "Vital signs monitoring during injectable and inhalant anesthesia in mice," Exp. Anim. **64**(1), 57–64 (2015).

58. A. Joseph, A. Guevara-Torres, and J. Schallek, "Imaging single-cell blood flow in the smallest to largest vessels in the living retina," eLife **8**, e45077 (2019).

59. A. Guevara-Torres, A. Joseph, and J. B. Schallek, "Label free measurement of retinal blood cell flux, velocity, hematocrit and capillary width in the living mouse eye," Biomed. Opt. Express **7**(10), 4228–4249 (2016).

60. M. D. Abràmoff, P. J. Magalhães, and S. J. Ram, "Image processing with imageJ," Biophotonics Int. **11**(7), 36–41 (2004).

61. P. Thévenaz, U. E. Ruttimann, and M. Unser, "A Pyramid Approach to Subpixel Registration Based on Intensity," IEEE Trans. on Image Process. **7**(1), 27–41 (1998).

62. R. J. Zawadzki, A. R. Fuller, S. S. Choi, D. F. Wiley, B. Hamann, and J. S. Werner, "Correction of motion artifacts and scanning beam distortions in 3D ophthalmic optical coherence tomography imaging," Proc. SPIE **6426**, 642607 (2007).

63. S. P. Collin and H. B. Collin, "Primary cilia in vertebrate corneal endothelial cells," Cell Biol. Int. **28**(2), 125–130 (2004).

64. M. H. Longair, D. A. Baker, and J. D. Armstrong, "Simple neurite tracer: Open source software for reconstruction, visualization and analysis of neuronal processes," Bioinformatics **27**(17), 2453–2454 (2011).

65. D. L. DeMill, M. Hussain, R. Pop-Busui, and R. M. Shtein, "Ocular surface disease in patients with diabetic peripheral neuropathy," Br. J. Ophthalmol. **100**(7), 924–928 (2016).

66. J. C. Erie, J. W. McLaren, D. O. Hodge, and W. M. Bourne, "The effect of age on the corneal subbasal nerve plexus," Cornea **24**(6), 705–709 (2005).

67. H. Ko, D. M. Snodderly, and M. Poletti, "Eye movements between saccades: Measuring ocular drift and tremor," Vision Res. **122**, 93–104 (2016).

68. A. Cruzat, Y. Qazi, and P. Hamrah, "In Vivo Confocal Microscopy of Corneal Nerves in Health and Disease," Ocul. Surf. **15**(1), 15–47 (2017).